Electronic Research Archive

Research article

Bifurcation and negative self-feedback mechanisms for enhanced spike-timing precision of inhibitory interneurons

Yanbing Jia[1], Huaguang Gu[2,*], Xianjun Wang[3], Yuye Li[4] and Chunhuizi Zhou[1]

[1] School of Mathematics and Statistics, Henan University of Science and Technology, Luoyang 471000, China
[2] School of Aerospace Engineering and Applied Mechanics, Tongji University, Shanghai 200092, China
[3] School of Mathematics and Science, Henan Institute of Science and Technology, Xinxiang 453003, China
[4] College of Mathematics and Computer Science, Chifeng University, Chifeng 024000, China

* **Correspondence:** Email: guhuaguang@tongji.edu.cn.

Abstract: A high spike-timing precision characterized by a small variation in interspike intervals of neurons is important for information processing in various brain functions. An experimental study on fast-spiking interneurons has shown that inhibitory autapses functioning as negative self-feedback can enhance spike-timing precision. In the present paper, bifurcation and negative self-feedback mechanisms for the enhanced spike-timing precision to stochastic modulations are obtained in two theoretical models, presenting theoretical explanations to the experimental finding. For stochastic spikes near both the saddle-node bifurcation on an invariant cycle (SNIC) and the subcritical Hopf (SubH) bifurcation with classes 1 and 2 excitabilities, respectively, enhanced spike-timing precision appears in large ranges of the conductance and the decaying rate of inhibitory autapses, closely matching the experimental observation. The inhibitory autaptic current reduces the membrane potential after a spike to a level lower than that in the absence of inhibitory autapses and the threshold to evoke the next spike, making it more difficult for stochastic modulations to affect spike timings, and thereby enhancing spike-timing precision. In addition, firing frequency near the SubH bifurcation is more robust than that near the SNIC bifurcation, resulting in a higher spike-timing precision for the SubH bifurcation. The bifurcation and negative self-feedback mechanisms for the enhanced spike-timing precision present potential measures to modulate the neuronal dynamics or the autaptic parameters to adjust the spike-timing precision.

1. Introduction

Under the influence of various modulations such as synaptic input, depolarizing current and noise, neurons can generate spike trains carrying neural information. The generation of spike trains and the transmission of spike trains among different neurons via synapses are important foundations for brain functions [1]. Since noise is ubiquitous in the nervous system [2], even under the same stimulus, the same neuron generates spike trains with variability, with a small variability corresponding to a higher spike-timing precision [3]. Experimental studies have shown that different types of neurons show different spike-timing precision. For example, in the neocortex of rats, GABAergic fast-spiking interneurons show more precise spike timing than pyramidal neurons [4]. Precise spike timing is identified to play important roles in the coding of sensory information including visual [3], auditory [5] and pain information [6]. Moreover, spike-timing precision is closely related to synchronized oscillations such as gamma oscillations which are associated with various physiological functions [7,8]. For instance, in hippocampal slice of mice, parvalbumin and somatostatin interneurons promote the precise spike timing of pyramidal neurons to form gamma oscillations [8]. Hence, identifying modulations of spike timing is very important for the recognition of brain functions.

An experimental study has shown that inhibitory autapses facilitate the spike-timing precision of neocortical GABAergic interneurons [4]. Autapses refer to special synapses that connect different parts of the same neuron. Autapses are widely present in different areas of the mammalian brain, such as the neocortex and the hippocampus [4,9]. Inhibitory autapses always suppress neural activities. For example, for basket cells in the human neocortex, inhibitory autapses prolong somatic inhibition after the spike and inhibit spiking [10]. However, inhibitory autapses can sometimes enhance neural activities. For instance, for interneurons in the mouse entorhinal cortex, inhibitory autapses can induce sustained spiking [11]. These experimental studies showed that the functions of inhibitory autapses in the real nervous system are complex. Moreover, theoretical studies demonstrated that autapses show complex and even counterintuitive influences on neuronal dynamics [12–17]. In single neurons, inhibitory autapses can induce the change from silence behavior to repetitive firing by post-inhibitory rebound [18], and inhibitory autapses with fast decaying rate can enhance the "Fold/Homoclinic" bursting activity [19]. In coupled receiver and sender neurons, inhibitory autapse can advance the spikes of the receiver neuron, leading to anticipated synchronization between the receiver and sender neurons [20]. In neuronal networks, inhibitory autapses can promote coherence resonance [21] and synchronized gamma oscillations [22]. These studies are important for identifying the functions of autapses. In these multiple studies [18–22], the autaptic dynamics underlying the modulations of autapses on the nervous system have been acquired, such as the fast or slow decaying rate and the strong or weak conductance of the autapses. Then, identifying the dynamics of inhibitory autapses is important for studying the enhanced spike-timing precision [4].

In these studies [18–22], except for the autaptic dynamics, the bifurcation of neurons underlying the modulations of autapses on the nervous system has also been obtained. The bifurcation or excitability of neurons in response to external stimuli is an important property of neurons. The excitability of neurons can be divided into classes 1, 2 and 3 according to the distinct responses of neurons

to external stimuli [23], among which classes 1 and 2 excitabilities have received much attention [24] and also have been related to different bifurcations. The main difference between classes 1 and 2 excitabilities is as follows: With increasing the applied current, neurons with class 1 excitability at the resting sate begin firing with an arbitrarily small (near zero) firing frequency, while neurons with class 2 excitability at the resting sate begin firing with a certain frequency [23]. In the theory of nonlinear dynamics, this difference is caused by that the classes 1 and 2 excitabilities are respectively related to the saddle–node bifurcation on an invariant circle (SNIC) and the Hopf bifurcation [23]. Neurons with classes 1 and 2 excitabilities always show different dynamics. For instance, neurons with classes 1 and 2 excitabilities show differences in phase responses induced by pulse stimuli [25], in stochastic firing patterns induced by noise [26,27] and in synchronization behaviors in neuronal networks [28]. Then, identifying the excitabilities or bifurcations of fast spiking interneurons is important for studying the enhanced spiking-timing precision [4].

In the present study, bifurcation of fast spiking interneurons and negative self-feedback mechanism of inhibitory autaptic current for enhanced spike-timing precision of inhibitory interneurons are obtained, presenting theoretical explanations to the experimental observation [4]. Two interneuron models are studied, including the Wang-Buzsáki (WB) model with class 1 excitability and the Erisir model with class 2 excitability [29], and the difference in spike-timing precision of classes 1 and 2 excitabilities are obtained. On the one hand, inhibitory autapses can promote spike-timing precision of the WB model near the SNIC bifurcation and of the Erisir model near the Hopf bifurcation. This is because inhibitory autapses decreases the after-spike potential lower than the threshold for generating action potentials, making it difficult for noise to induce spike timings with large variability. On the other hand, the spike-timing precision of the Erisir model is higher than that of the WB model, since the firing frequency near the Hopf bifurcation of the Erisir model exhibits lower increasing rate than that near the SNIC bifurcation of the WB model. The bifurcation and negative self-feedback mechanism for the enhanced spike-timing precision provide potential means to modulate the neuronal dynamics or the autaptic parameters to adjust the spike-timing precision.

The rest of this paper is organized as follows. In Section 2, the models and methods are introduced. In Section 3, the results and the corresponding interpretations are presented. In Section 4, the conclusions and discussions are given.

2. Models and methods

2.1. Interneuron models

Two models of interneurons, including the Erisir and WB models, are used in the present study. The Erisir and WB models are often used to simulate the firing activity of interneurons in the neocortex and hippocampus of mice or rats, respectively [29]. Both the Erisir and WB models are described as follows:

$$
\begin{cases}
C\dfrac{dV}{dt} = g_{Na}m_\infty^3(V)h(V_{Na}-V) + g_K n^x(V_K-V) + g_L(V_L-V) + I_{app} \\
\dfrac{dh}{dt} = \varphi\left[\alpha_h(V)(1-h) - \beta_h(V)h\right] \\
\dfrac{dn}{dt} = \varphi\left[\alpha_n(V)(1-n) - \beta_n(V)n\right]
\end{cases}, \qquad (1)
$$

The variable V represents the membrane potential. The variables h and n are gating variables of the sodium (Na$^+$) and potassium (K$^+$) channels, respectively. The parameter C stands for the membrane capacitance. The parameters g_{Na}, g_K and g_L respectively denote the maximal conductances of the Na$^+$, K$^+$ and leak currents and V_{Na}, V_K and V_L represent the corresponding reversal potentials. The parameter x is the power of the variable n and the parameter φ controls the inactivation or activation rate of the Na$^+$ and K$^+$ channels. Both x and φ are dimensionless. The parameter I_{app} stands for the applied current, which is selected as a control parameter. The other parameters are fixed, as shown in Table 1.

Table 1. Parameters of the Erisir and WB models.

	C (μF/cm^2)	x	φ	g_{Na} (mS/cm^2)	g_K (mS/cm^2)	g_L (mS/cm^2)	V_{Na} (mV)	V_K (mV)	V_L (mV)
Erisir	1	2	1	112	224	0.5	60	−90	−70
WB	1	4	5	35	9	0.1	55	−90	−65

For the Erisir model, the functions are as follows: $m_\infty(V) = \alpha_m(V)/[\alpha_m(V)+\beta_m(V)]$, $\alpha_m(V) = 40(75.5-V)/\{\exp[(75.5-V)/13.5]-1\}$, $\beta_m(V) = 1.2262/[\exp(V/42.248)]$, $\alpha_h(V) = 0.0035/[\exp(V/24.186)]$, $\beta_h(V) = -0.017(V+51.25)/\{\exp[-(V+51.25)/5.2]-1\}$, $\alpha_n(V) = (95-V)/\{\exp[(95-V)/11.8]-1\}$, $\beta_n(V) = 0.025/[\exp(V/22.222)]$.

For the WB model, the functions are as follows: $m_\infty(V) = \alpha_m(V)/[\alpha_m(V)+\beta_m(V)]$, $\alpha_m(V) = 0.1(V+35)/\{1-\exp[-0.1(V+35)]\}$, $\beta_m(V) = 4\exp[-(V+60)/18]$, $\alpha_h(V) = 0.07\exp[-(V+58)/20]$, $\beta_h(V) = 1/\{\exp[-0.1(V+28)]+1\}$, $\alpha_n(V) = 0.01(V+34)/\{1-\exp[-0.1(V+34)]\}$, $\beta_n(V) = 0.125\exp[-(V+44)/80]$.

2.2. Interneuron models with Gaussian white noise and inhibitory autapses

Inhibitory autapses and Gaussian white noise are introduced to the interneuron models as follows:

$$\begin{cases} C\dfrac{dV}{dt} = g_{Na}m_\infty^3(V)h(V_{Na}-V) + g_K n^x(V_K-V) + g_L(V_L-V) + I_{app} + I_{aut} + \xi(t) \\ \dfrac{dh}{dt} = \varphi\left[\alpha_h(V)(1-h) - \beta_h(V)h\right] \\ \dfrac{dn}{dt} = \varphi\left[\alpha_n(V)(1-n) - \beta_n(V)n\right] \end{cases} , \qquad (2)$$

where I_{aut} represents the autaptic current which is described as follows:

$$I_{aut} = gs(V_{aut}-V). \qquad (3)$$

The variable s stands for the channel opening fraction of the autapses, the parameter g denotes the conductance and V_{aut} represents the reversal potential. For the Erisir and WB models, V_{aut} is respectively fixed at –88 mV and –75 mV to obtain inhibitory autaptic currents. The variable s is modeled as follows [30]:

$$\frac{ds}{dt} = \alpha \frac{1}{1+\exp\left[-0.5\left(V-\theta\right)\right]}\left(1-s\right)-\frac{1}{\tau}s \qquad (4)$$

where parameters α, θ and τ represent the channel opening rate, the threshold and the decay time of the autapses, respectively. In the present paper, $\alpha = 12$ ms^{-1} and $\theta = 0$ mV and g and τ are control parameters.

To induce variations in spike timings, Gaussian white noise $\xi(t)$ is introduced to Eq (2) with statistical properties $\langle\xi(t)\rangle = 0$ and $\langle\xi(t)\xi(t')\rangle = 2D\delta(t-t')$, in which D stands for the noise intensity and δ represents Dirac delta function. In this study, unless otherwise stated, D is set as 0.3 pA/cm^2. Other values of D do not influence the results in the present study qualitatively.

2.3. Methods

All models are simulated by the Euler method with an integration step of 0.001 ms. Bifurcation diagrams are acquired by XPPAUT software [31].

3. Results

3.1. Different bifurcations and different changing rates of the firing frequency for the two models

For the Erisir and WB models, with increasing I_{app}, bifurcation diagrams and changes of the firing frequency are presented in Figure 1. The Erisir model has several bifurcation points, as displayed in Figure 1(a1). As I_{app} increases, the stable focus (black solid line) becomes unstable (black dashed line) through a subcritical Hopf (SubH) bifurcation at $I_{app} = 7.01$ μA/cm^2, and the unstable limit circle (red dotted line) disappears at the same time. Moreover, there is a saddle-node bifurcation of limit cycles (SNLC) at $I_{app} = 6.48$ μA/cm^2, where the stable limit cycle (red solid lines) intersects with the unstable limit cycle (red dotted line). The unstable limit cycle (red dotted line) associated with the SNLC terminates at $I_{app} = 6.65$ μA/cm^2 via a homoclinic bifurcation (Hom1) and the unstable limit cycle associated with the SubH terminates at $I_{app} = 6.89$ μA/cm^2 also via a homoclinic bifurcation (Hom2). The two turning points of the curve of the equilibrium point (black dashed curve) are two saddle-node bifurcation points. The stable focus and stable limit cycle correspond to the resting state and spiking, respectively.

The Erisir model begins firing at the SubH bifurcation with the firing frequency approximately equaling 62.39 Hz, as shown in Figure 1(a2). Then, as I_{app} increases, the firing frequency increases and the increasing rate near the SubH bifurcation is relatively small, which is a characteristic of the class 2 excitability. For example, for $I_{app} = 7.3$ μA/cm^2 near the SubH bifurcation, the firing frequency is about 70 Hz, which is consistent with the firing frequency of interneurons in the neocortex of rats [4]. The increasing rate of the firing frequency at $I_{app} = 7.3$ μA/cm^2 is about $K_E \approx 25$ Hz/μA/cm^2, which is determined by the slope of the tangent line at $I_{app} = 7.3$ μA/cm^2, as illustrated by the red dashed line in Figure 1(a2). As I_{app} increases, the slope of the tangent line decreases, implying that the increasing rate of the firing frequency decreases, as shown in Figure 1(a3). In the present paper, $I_{app} = 0$ μA/cm^2 is used to simulate the resting state, and a step current with $I_{app} = 7.3$ μA/cm^2 is used to induce spiking from the resting state to study the spike-timing precision.

As shown in Figure 1(b1), a SNIC bifurcation appears at $I_{app} \approx 0.16$ μA/cm^2 in the WB model. As

I_{app} increases, the stable node (black solid) merges with the saddle (black dotted) and meanwhile an invariant cycle (red solid) corresponding to the spiking appears. The turning point of the curve of the equilibrium point (black dashed) is a saddle-node bifurcation. The stable node corresponds to the resting state. The invariant cycle exhibits infinite period corresponding to the firing frequency with 0 Hz. Therefore, with the increase of I_{app}, the firing frequency near the SNIC point increases relatively fast from 0 Hz, as shown in Figure 1(b2), which is a characteristic of the class 1 excitability. For example, for $I_{app} = 1.2$ μA/cm^2 near the SNIC at $I_{app} \approx 0.16$ μA/cm^2, the firing frequency is ~70 Hz with a fast increasing rate, as shown in Figure 1(b2). The increasing rate at $I_{app} = 1.2$ μA/cm^2 is $K_W \approx 45$ Hz/μA/cm^2, as illustrated by the red dashed line in Figure 1(b2). As I_{app} increases, the slope of the tangent line also decreases, implying that the increasing rate of the firing frequency decreases, as depicted in Figure 1(b3). In the present study, $I_{app} = 0$ μA/cm^2 is used to simulate the resting state, and a step current with $I_{app} = 1.2$ μA/cm^2 is used to induce spiking from the resting state to study the spike-timing precision.
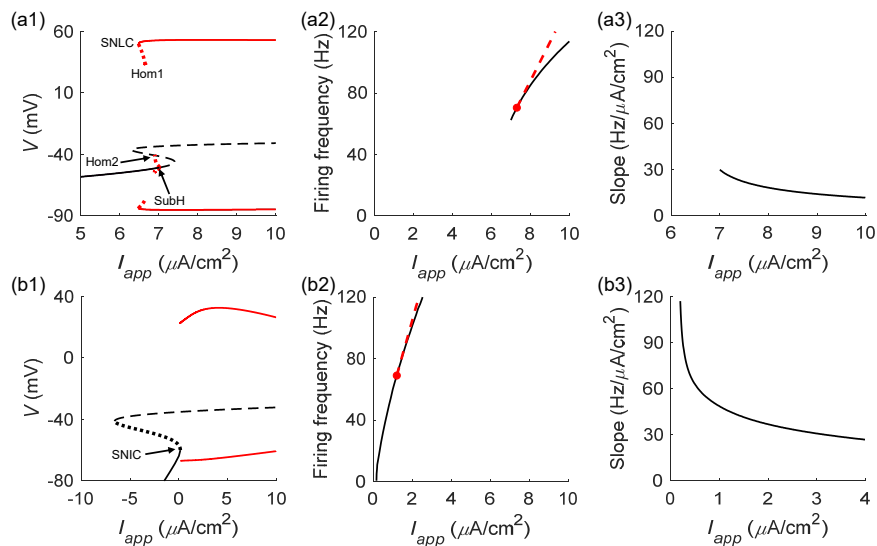

Figure 1. Dynamics of the Erisir model (top) and the WB model (bottom). (a1) and (b1) Bifurcation diagrams. (a2) and (b2) Dependence of the firing frequency on the applied current I_{app}. The red dashed lines are tangent lines respectively at $I_{app} = 7.3$ μA/cm^2 and $I_{app} = 1.2$ μA/cm^2 with the firing frequency of ~70 Hz. (a3) and (b3) Dependence of the slope of the tangent line on the applied current I_{app}.

As shown in Figure 1(a3) and (b3), the slope of the Erisir model is smaller (always below 30 Hz/μA/cm^2), whereas the slope of the WB model is larger (always above 30 Hz/μA/cm^2), implying that the increasing rate of the firing frequency of the Erisir model always smaller than that of the WB model. In addition, since $K_E \approx 25$ Hz/μA/cm^2 is much smaller than $K_W \approx 45$ Hz/μA/cm^2, the increasing rate of the firing frequency of the Erisir model near $I_{app} = 7.3$ μA/cm^2 is much smaller than that of the WB model near $I_{app} = 1.2$ μA/cm^2. Thus, it can be speculated that spikes of the Erisir model should be more robust than that of the WB model. That is, the WB model should show lower spike-timing precision than the Erisir model, which will be addressed in detail in the following subsections.

3.2. Spike-timing precision characterized by spike jitter and coefficient variation

Similar to the experimental study [4], a step current is used to induce the interneuron models to generate spiking. For the deterministic Erisir model without inhibitory autapse, when I_{app} (red) changes from 0 to 7.3 µA/cm^2 at $t = 20$ ms, the neuronal activity (black) changes from resting state to spiking with the firing rate of ~70 Hz, as shown in Figure 2(a1). Similarly, for the deterministic WB model without inhibitory autapse, when I_{app} (red) changes from 0 to 1.2 µA/cm^2, the neuronal activity (black) also changes from resting state to spiking with the firing rate of ~70 Hz, as shown in Figure 2(b1).
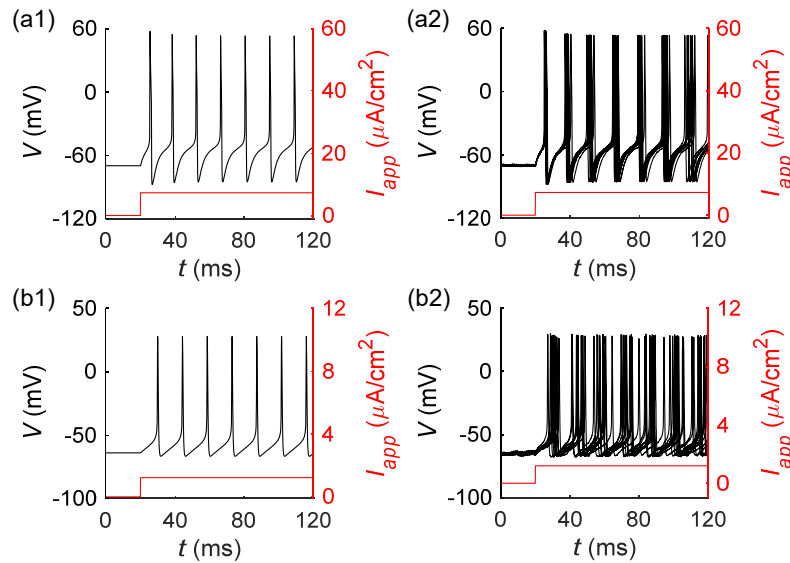

Figure 2. Spiking (black) of the deterministic and stochastic models without autapses induced by a step current (red). (a1) Spiking of the deterministic Erisir model. (a2) Ten trials of spiking of the stochastic Erisir model. (b1) Spiking of the deterministic WB model. (a2) Ten trials of spiking of the stochastic WB model. In (a2) and (b2), the noise intensity D is 0.1 pA/cm^2.

Noises with the same intensities but different time courses are introduced to the deterministic model in Figure 2(a1) to form different trials, as indicated by different black lines in Figure 2(a2). Compared with the i-th spike in Figure 2(a1), the i-th spikes in different trials ($N = 10$ trials are shown here) in Figure 2(a2) exhibit a variation in spike timings. A small degree of variation corresponds to a high spike timing precision. Similarly, different trials of the stochastic WB model are presented in Figure 2(b2), showing a lower spike-timing precision than the Erisir model.

Similar to the experimental study [4], two measures are employed to characterize the spike-timing precision. One is the spike jitter, and the other is coefficient variation (CV) of interspike intervals (ISIs). Jitter of the i-th spikes (labeled as J_i, $i = 1, 2, 3, \ldots$) is quantified as the standard deviation (SD) of the spike timings. That is,

$$J_i = \sqrt{\frac{1}{N-1} \sum_{j=1}^{N} \left(T_{ij} - \overline{T_i} \right)^2}, \tag{5}$$

where N is the number of trials, T_{ij} denotes the spike timing of the i-th spike in the j-th trial and $\overline{T_i} = \sum_{j=1}^{N} T_{ij} / N$ stands for the mean spike timing of the i-th spikes in N trials.

For example, for the stochastic Erisir and WB models described as Eq (2), the dependence of jitter of the i-th spikes (J_i) on $\overline{T_i}$ for different g values when $\tau = 4$ ms are respectively depicted in Figure 3(a) and (b). For each model and a fixed g value, J_i increases with increasing $\overline{T_i}$, which is similar to the experimental result [4]. With increasing g, J_i decreases, indicating that spike-timing precision increases with the increase in g. Thus, J_i is a suitable indicator for measuring the spike-timing precision. Moreover, J_i for the Erisir model is lower than that for the WB model, indicating that the Erisir model shows higher spike-timing precision than the WB model. This difference in spike-timing precision is induced by different changing rates of the firing frequency or by different excitabilities or bifurcations, which will be addressed in Subsection 3.5.
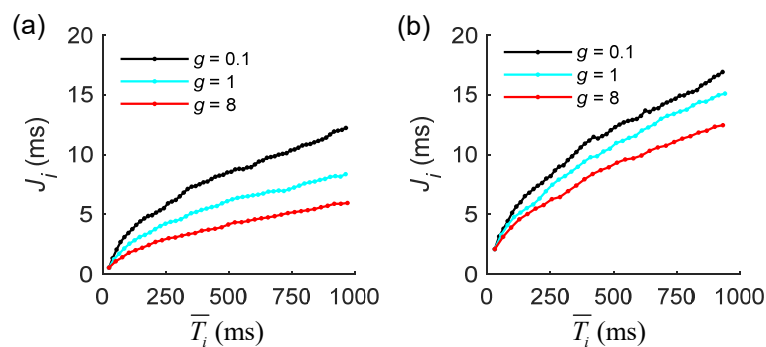

Figure 3. The dependence of jitter of the i-th spikes (J_i) on the mean spike timing of the i-th spikes ($\overline{T_i}$) for different g values when $\tau = 4$ ms. (a) The Erisir model; (b) The WB model. The number of trials is $N = 10$.

Although the change of J_i with respect to $\overline{T_i}$ can reveal the difference in spike-timing precision under different parameters, it is not convenient to be used to characterize the dependence of spike-timing precision on two parameters or the distribution of spike-timing precision on a parameter plane. Then, mean jitter over all spikes (labeled as J) is considered as follows:

$$J = \frac{1}{M} \sum_{i=1}^{M} J_i ,\tag{6}$$

where M stands for the total number of spikes. J can be employed to describe the dependence of spike-timing precision on two parameters, and a smaller J corresponds to a higher spike-timing precision.

In addition, CV of all ISIs is considered, where the number of all ISIs is $M \times N$, as there are N trials and each trial has M ISIs. CV is quantified as the ratio of the SD of all ISIs to the mean of all ISIs, and a smaller CV corresponds to a higher spike-timing precision.

In the present study, to ensure a high accuracy, $N = 200$ and $M = 500$ are used to calculate the mean spike jitter J and CV of ISIs.

3.3. Inhibitory autapses reduce the firing rate of deterministic interneuron model

The dependence of ISIs of the deterministic Erisir (left) and WB (right) models on parameters g

and τ is depicted in Figure 4. For the two models, long ISIs (red and yellow) appear at the upper right of the parameter plane, while short ISIs (blue) locate at the bottom and left part, indicating that ISIs of the two interneuron models increase with increasing g or τ. That is, inhibitory autapses reduce the firing rate of the two interneuron models.
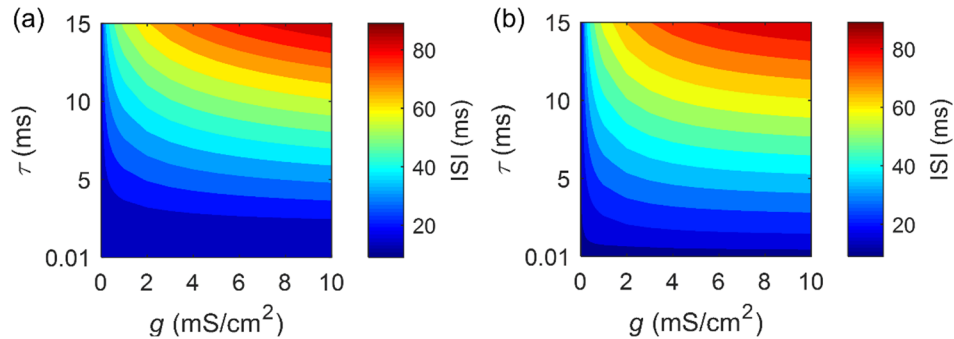

Figure 4. Dependence of ISIs of deterministic interneuron models on g and τ. (a) The Erisir model; (b) The WB model.

3.4. Influence of inhibitory autapses on spike-timing precision

3.4.1. Autapses enhance spike-timing precision characterized by J within a large parameter range

For the Erisir model, the dependence of mean jitter J on g and τ is displayed in Figure 5(a1). Obviously, small J values (blue) corresponding to large spike-timing precision appear in the middle right that covers most regions of the (g, τ) parameter plane. Large J values (red, yellow and green) corresponding to small spike-timing precision appear in the upper left and the bottom of the parameter plane. The horizontal dashed line represents $\tau = 4$ ms of the inhibitory autapse, which is consistent with the experimental study showing that the decay time of inhibitory autaptic currents of interneurons in the neocortex of mice is approximately 4 ms [32]. For the WB model, the dependence of J on g and τ is presented in Figure 5 (b1). Small J values (light blue) corresponding to large spike-timing precision appear in the middle right of the parameter plane. Large J values (red, yellow and green) corresponding to small spike-timing precision appear in the left and the bottom of the parameter plane. The distributions of J in the (g, τ) parameter plane for the two models are different to a certain extent. For the Erisir model with a large g value, J first decreases and then increases with increasing g. For the WB model with a large g value, J decreases with increasing g. In addition, J values of the Erisir model are lower than those of the WB model, which is addressed in detail in Subsection 3.5.

To show the influence of autapses on spike-timing precision, the difference in J between each model with and without autapse, labeled as ΔJ, is considered. The dependence of ΔJ on g and τ is depicted in Figure 5(a2) and (b2), where purple and blue ($\Delta J < -0.1$ ms), green (-0.1 ms $\leq \Delta J \leq 0.1$ ms) and yellow and red ($\Delta J > 0.1$ ms) represent enhanced, nearly unchanged and reduced spike-timing precision, respectively, after introducing inhibitory autapses to the models. For both models, spike-timing precision is enhanced in a large range (purple and blue) with large g values, as displayed in Figure 5(a2) and (b2), indicating that autapses enhance spike-timing precision of both models within a large parameter range. This result closely matches the experimental result that inhibitory autapses enhance spike-timing precision of neocortical interneurons [4]. However, for both models, spike-

timing precision is reduced in small regions (red and yellow). Distributions of regions with enhanced and reduced spike-timing precision are different to a certain extent for the two models. The obvious difference is that the top of the (g, τ) parameter plane shows reduced spike-timing precision (red and yellow) for the Erisir model while not for the WB model. This may because the ISIs of the Erisir model become long at the upper left of the parameter plane and long ISIs could sensitively increase spike jitter of the Erisir model. In addition, for both models, other regions with reduced spike-timing precision (red and yellow) locate at the left and bottom of the parameter plane.
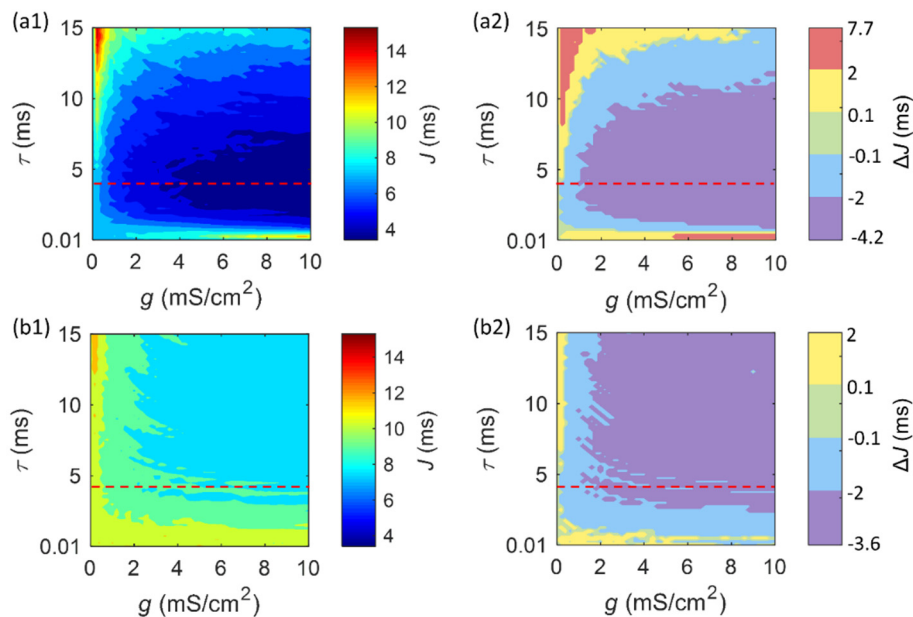

Figure 5. Dependence of J (left) and ΔJ (right) on g and τ. (a1) and (a2) The Erisir model; (b1) and (b2) The WB model. The horizontal dashed lines denote $\tau = 4$ ms.

3.4.2.   Autapses enhance spike-timing precision quantified by adjusted J within a large parameter range

As depicted in Figure 4, ISIs of both the Erisir and WB models increase with increasing g or τ. To illustrate the influence of ISIs or firing frequency on the phenomenon of enhanced spike-timing precision induced by autapses, each J value in Figure 5(a1) and (b1) is adjusted by the mean ISI of all trials. That is, the ratio of J to the mean ISI is considered.

For the Erisir and WB models, the dependence of the adjusted J, labeled as AJ, on g and τ are depicted in Figure 6(a1) and (b1), respectively. The distributions of AJ in the (g, τ) parameter plane for the two models are similar to a large extent. Small AJ values (blue) corresponding to large spike-timing precision appear in the upper right that covers most regions of the (g, τ) parameter plane. Large AJ values (red, yellow and green) corresponding to small spike-timing precision appear in the left and the bottom of the parameter plane. Moreover, for each model, the region with large spike-timing precision (blue) becomes wider after adjusting J, as shown in Figure 6(a1) and (b1).

The difference in AJ of each model in the presence and in the absence of autapse, labeled as ΔAJ, is then considered. The dependence of ΔAJ on g and τ is depicted in Figure 6(a2) and (b2), where purple and blue ($\Delta AJ < -0.01$), green ($-0.01 \leq \Delta AJ \leq 0.01$) and yellow and red ($\Delta AJ > 0.01$) represent enhanced, nearly unchanged and reduced spike-timing precision, respectively, after introducing inhibitory autapses to the

models. As shown in Figure 6(a2) and (b2), for both models, spike-timing precision is enhanced in a large range (purple and blue) at the upper right, while is reduced in a small range at the bottom (red and yellow). The results indicate that the phenomenon of the enhanced spike-timing precision induced by inhibitory autapses is not dependent on ISIs or firing frequency.
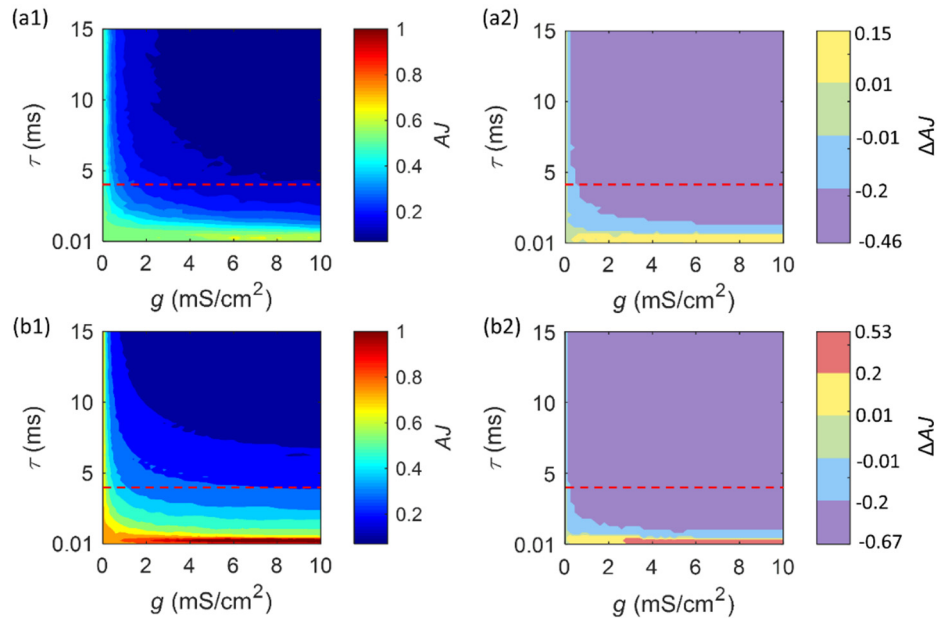

Figure 6. Dependence of *AJ* (left) and ΔAJ (right) on *g* and τ. (a1) and (a2) The Erisir model; (b1) and (b2) The WB model. The horizontal dashed lines denote $\tau = 4$ ms.

3.4.3. Autapses enhance spike-timing precision characterized by CV within a large parameter range

The dependence of CV of ISIs on *g* and τ for the Erisir model is depicted in Figure 7(a1) and for the WB model in Figure 7(b1). For both models, regions with large CV values (red, yellow and green) corresponding to small spike-timing precision appear in the bottom and left part of the parameter plane (g, τ), whereas regions with small CV values (blue) corresponding to large spike-timing precision appear in the upper right of the parameter plane. However, the variation of CV with increasing τ is different for the two models. For a fixed *g* value, as τ increases, CV of the Erisir model first decreases and then increases, whereas CV of the WB model decreases monotonously. Moreover, CV values of the Erisir model are lower than those of the WB model, which will be further addressed in Subsection 3.5.

The dependence of the difference in CV (labeled as ΔCV) between each model with and without autapse on *g* and τ is presented in Figure 7(a2) and (b2), where purple and blue ($\Delta CV < -0.01$), green ($-0.01 \leq \Delta CV \leq 0.01$) and yellow and red ($\Delta CV > 0.01$) represent enhanced, nearly unchanged and reduced spike-timing precision, respectively, after introducing inhibitory autapses to the models. For both models, regions with enhanced spike-timing precision (purple and blue) appear in the upper right and cover most parts of the (g, τ) parameter plane, as depicted in Figure 7(a2) and (b2), showing that autapses enhance spike-timing precision of both models within a large parameter range. For both models, regions with reduced spike-timing precision (red and yellow) locate at the left and the bottom of the parameter plane. Such distributions are similar to the results of ΔJ in Figure 5(b2). However, both the bottom and the left regions of the WB model are smaller than those of the Erisir model.
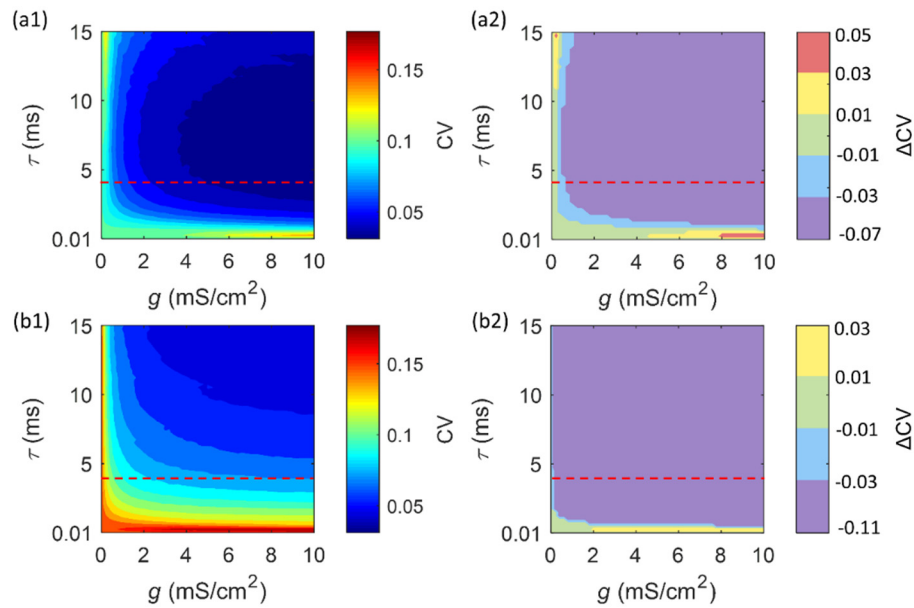
Figure 7. Dependence of CV (left) and ΔCV (right) on g and τ. (a1) and (a2) The Erisir model; (b1) and (b2) The WB model. The horizontal dashed lines denote $\tau = 4$ ms.

3.5. Spike-timing precision of the Erisir model is larger than that of the WB model

In this subsection, both J and CV are employed to study the difference in spike-timing precision between the Erisir and WB models with different bifurcations and changing rates of the firing frequency.

For the mean jitter J, the difference (denoted as DJ) acquired by subtracting J values of the WB model (Figure 5(b1)) from those of the Erisir model (Figure 5(a1)), is illustrated in Figure 8(a). In Figure 8(a), purple (DJ < –0.1 ms), green (–0.1 ms ≤ DJ ≤ 0.1 ms) and red (DJ > 0.1 ms) represent that spike-timing precision of the Erisir model is larger than, almost equal to and smaller than that of the WB model, respectively. For CV of ISIs, the difference (labeled as DCV) acquired by subtracting CV values of the WB model (Figure 7(b1)) from that of the Erisir model (Figure 7(a1)), is illustrated in Figure 8(b). In Figure 8(b), purple (DCV < –0.001), green (–0.001 ≤ DCV ≤ 0.001) and red (DCV > 0.001) represent that spike-timing precision of the Erisir model is larger than, almost equal to and smaller than that of the WB model, respectively.
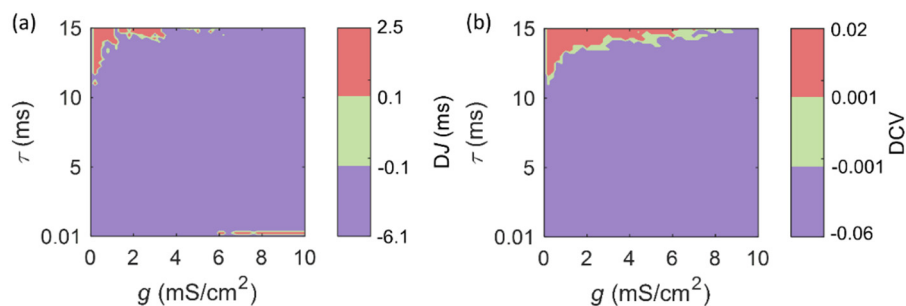

Figure 8. The difference in precise spike timing between the Erisir model and the WB model. (a) DJ; (b) DCV.

For both DJ and DCV, except for a small region at the up-left corner of the parameter plane (red and green), in a large region of the parameter plane (purple), the spike-timing precision of the Erisir model is larger than that of the WB model, as shown in Figure 8(a) and (b). This is in line with the speculation acquired by different changing rates of the firing frequency of the two models in Subsection 3.1, which can be explained as follows. The increasing rate of the firing frequency of the Erisir model near $I_{app} = 7.3$ μA/cm^2 ($K_E \approx 25$ Hz/μA/cm^2) is much smaller than that of the WB model near $I_{app} = 1.2$ μA/cm^2 ($K_W \approx 45$ Hz/μA/cm^2), leading to that the firing activity of the WB model is more sensitive to external stimuli than that of the Erisir model. Therefore, for Gaussian white noise with the same intensity, the firing regularity or the precise spike timing of the Erisir model is higher than that of the WB model.

3.6. Inhibitory autapses with $\tau = 4$ ms enhance spike-timing precision

An experimental study has shown that the decay time τ of inhibitory autaptic currents of interneurons in the neocortex of mice is approximately 4 ms [32]. As an example, we then investigate the impact of inhibitory autapses with $\tau = 4$ ms on spike-timing precision of the Erisir and WB models. The red dashed lines in Figures 5 and 7 denote $\tau = 4$ ms.

When $\tau = 4$ ms, for both models, the dependence of J and CV on g is displayed in Figure 9(a) and (b), respectively. J or CV of each model decreases with increasing g, indicating that inhibitory autapses promote spike-timing precision of each model. This is in accordance with the results in Figures 5 and 7 that autapses enhance spike-timing precision within a large parameter range. In addition, for a fixed g value, J or CV of the Erisir model is smaller than that of the WB model. That is, the Erisir model shows more precise spike timing than the WB model, which is in line with the results in Figure 8, that the Erisir model shows more precise spike timing than the WB model within a large parameter range.
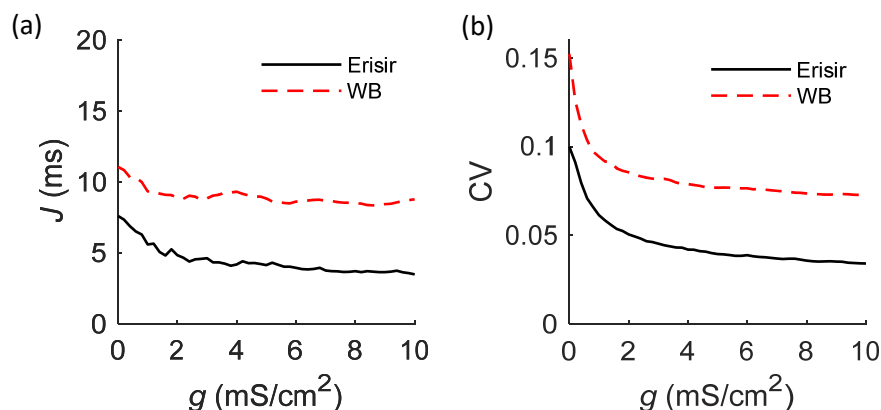

Figure 9. The dependence of mean jitter J and CV of ISIs on g when $\tau = 4$ ms. (a) J and (b) CV.

For the Erisir model and the WB model, the firing activity for different g values when $\tau = 4$ ms is presented in Figure 10. As g increases, the variation of the i-th spikes decreases, i.e., the jitter of the i-th spikes decreases.
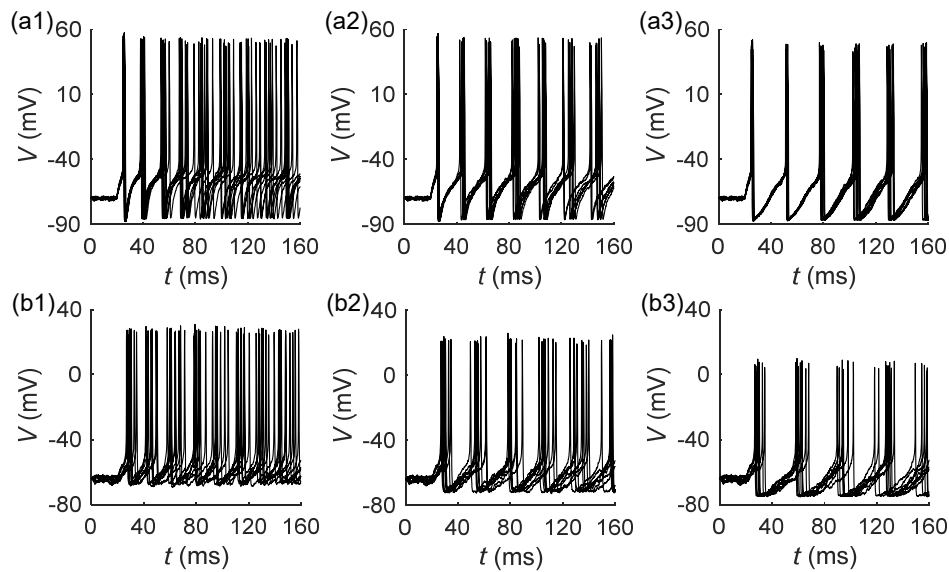
Figure 10. Ten trials of the spiking of the Erisir model (top) and the WB model (bottom) for different g values when $\tau = 4$ ms. (a1) and (b1) $g = 0.1$ mS/cm^2; (a2) and (b2) $g = 1$ mS/cm^2; (a3) and (b3) $g = 8$ mS/cm^2.

3.7. Mechanisms of inhibitory autaptic current for the enhanced spike-timing precision

To explain why autapses enhance spike-timing precision or firing regularity of the Erisir model, inhibitory autapse with $\tau = 4$ ms is chosen as a representative example. Two trials for $g = 0.1$ and 1 mS/cm^2 are illustrated in Figure 11. The membrane potential (V) and the corresponding inhibitory autaptic current (I_{aut}) are shown in each panel of Figure 11(a) and (b). To show the detailed relationship between V and $I_{aut} = gs(V_{aut}-V)$, partial enlarged view of Figure 11(b) in a period is shown in Figure 11(c). As V crosses the autaptic threshold $\theta = 0$ mV, I_{aut} begins to increase from a low level near zero. After V reaching its maximal value, I_{aut} decays to a low level with the decaying rate determined by τ, as shown in Figure 11(c).

To compare the time courses between the two g values, the time indicated by the dashed black lines where V crosses the autaptic threshold $\theta = 0$ mV in Figure 11(a) and (b) is set as the same initial time of a period. The autaptic currents for $g = 0.1$ and 1 mS/cm^2 are presented in Figure 11(d), and the membrane potentials for $g = 0.1$ and 1 mS/cm^2 are shown in Figure 11(e). As g increases from 0.1 to 1 mS/cm^2, the autaptic current becomes stronger during the spike and the after-spike potential, as depicted in Figure 11(d). This leads to that the after-spike potential on the left of phase C is lower than that of phase B, where phases B and C respectively denote the thresholds for evoking spikes for $g = 0.1$ and 1 mS/cm^2, as shown in Figure 11(e). The phase trajectories of the spikings for $g = 0.1$ and 1 mS/cm^2 are shown Figure 11(f). Obviously, the phase trajectory before the phase B for $g = 0.1$ mS/cm^2 (black) is closer to the threshold, compared with the phase trajectory before the phase C for $g = 1$ mS/cm^2 (red). Then, the membrane potential before phase B is more sensitive to noise, i.e., larger variations around phase B for $g = 0.1$ mS/cm^2 and smaller variations around phase C for $g = 1$ mS/cm^2, resulting in enhanced spike-timing precision for larger g values. Moreover, since the decreased after-spike potential needs more time to recover to the threshold for evoking spikes, the ISI increases, as illustrated in Figure 11(b). Similar to the Erisir model, the increase in spike-timing precision of the WB model by inhibitory autapse with

$\tau = 4$ ms is also caused by the decreased after-spike potential, as shown in Figure 12.
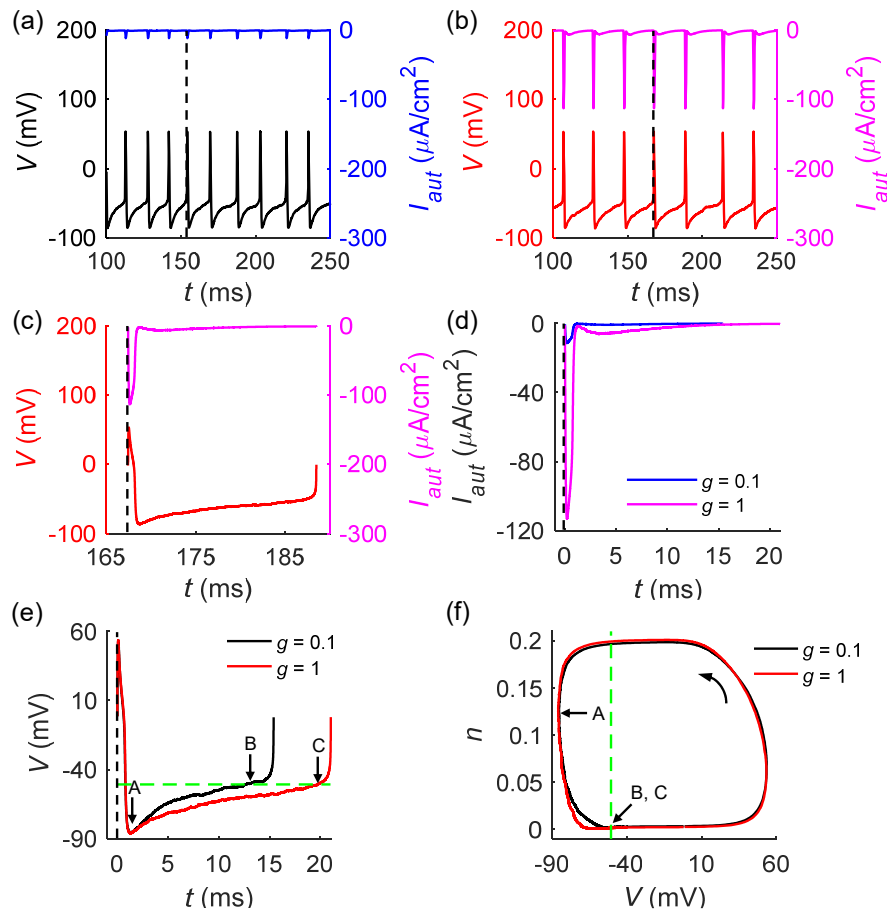

Figure 11. The membrane potential (V) and the autaptic current (I_{aut}) of the Erisir model for different g values. (a) V (black) and I_{aut} (blue) for $g = 0.1$ mS/cm^2; (b) V (red) and I_{aut} (magenta) for $g = 1$ mS/cm^2; (c) Partial enlarged view of panel (b); (d) I_{aut} for $g = 0.1$ mS/cm^2 (blue) and 1 mS/cm^2 (magenta); (e) V for $g = 0.1$ mS/cm^2 (black) and 1 mS/cm^2 (red); (f) The phase portrait for $g = 0.1$ mS/cm^2 (black) and 1 mS/cm^2 (red). In panels (a)–(e), the vertical dashed black lines mark the time where V crosses the autaptic threshold $\theta = 0$ mV. In panels (e) and (f), the dashed green line denotes the threshold of V, phase A marks the minimal value of the V and phases B and C mark V values crossing the threshold for $g = 0.1$ and 1 mS/cm^2, respectively.

4. Conclusions and discussions

Spike-timing precision is important for multiple brain functions. In the present paper, bifurcation of interneurons and negative self-feedback mechanism of inhibitory autapses for the enhanced spike-timing precision to stochastic modulations are obtained, which present theoretical explanations to the experimental finding of fast spiking interneurons [4]. The results in this study show significances in two aspects.
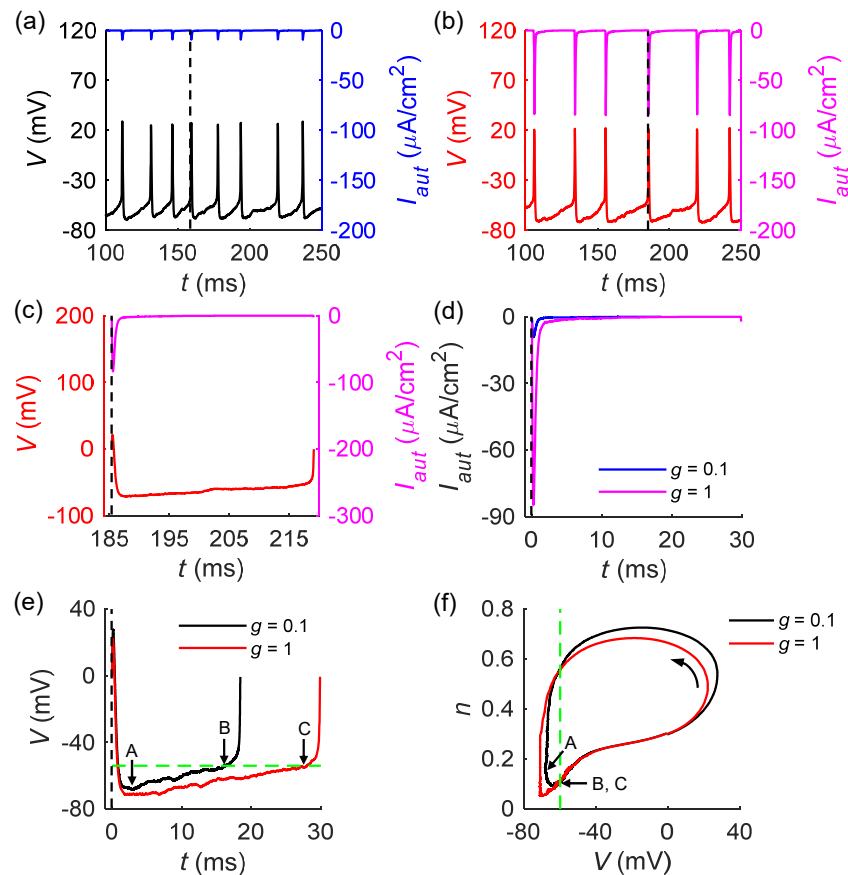
Figure 12. The membrane potential (V) and the autaptic current (I_{aut}) of the WB model for different g values. (a) V (black) and I_{aut} (blue) for $g = 0.1$ mS/cm^2; (b) V (red) and I_{aut} (magenta) for $g = 1$ mS/cm^2; (c) Partial enlarged view of panel (b); (d) I_{aut} for $g = 0.1$ mS/cm^2 (blue) and 1 mS/cm^2 (magenta); (e) V for $g = 0.1$ mS/cm^2 (black) and 1 mS/cm^2 (red); (f) The phase portrait for $g = 0.1$ mS/cm^2 (black) and 1 mS/cm^2 (red). In panels (a)–(e), the vertical dashed black lines mark the time where V crosses the autaptic threshold $\theta = 0$ mV. In panels (e) and (f), the dashed green line denotes the threshold of V, phase A marks the minimal value of the V and phases B and C respectively mark V values crossing the threshold for $g = 0.1$ and 1 mS/cm^2.

The influence of inhibitory autapses on spike-timing precision of two interneuron models including the WB and Erisir models is investigated. It is shown that spike-timing precision of both interneuron models is enhanced by inhibitory autapses within large ranges of the conductance and decay time. This phenomenon is caused by that inhibitory autapses decrease the after-spike potential much lower than the threshold for evoking spikes, making it difficult for noise to induce spike timings with large variability, thereby enhancing spike-timing precision of interneuron models. Thus, the present study provides a theoretical explanation to the experimental finding that inhibitory autapses can promote spike-timing precision of neocortical GABAergic interneurons, which helps to understand the importance of precise spike timing for correct sensory representation and cortical network oscillations [4]. The suppression effect of inhibitory autapses on the membrane potential in this study is in accordance with the previous study [33]. However, in many previous studies, the paradoxical influences of inhibitory autapses on dynamics of single neurons and neuronal networks were investigated [18–22]. For example, inhibitory autapses can promote

electrical activities in single neurons [18], and enhance coherence resonance [21] and synchronized gamma oscillations [22] in neuronal networks. These results along with the results in the present study help to reveal multiple functions of inhibitory autapses.

Moreover, the difference in spike-timing precision of the WB model with class 1 excitability and of the Erisir model with class 2 excitability is investigated. It is demonstrated that the Erisir model always shows higher spike-timing precision than the WB model. This phenomenon is caused by that the firing activity of the WB model near the SNIC bifurcation is more sensitive to noise than that of the Erisir model near the SubH bifurcation, manifested as a larger increasing rate of the firing frequency of the WB model than that of the Erisir model. The differences in dynamics of neurons with classes 1 and 2 excitabilities were also examined in previous studies. For instance, single neurons with classes 1 and 2 excitabilities show differences in phase responses induced by pulse stimuli [25] and in stochastic firing patterns induced by noise [26,27], and neuronal networks respectively composed of neurons with classes 1 and 2 excitabilities show differences in synchronization behaviors [28]. These results along with the results in the present study help to understand the difference in dynamics between neurons with classes 1 and 2 excitabilities. Considering that inhibitory autaptic transmission shows short-term plasticity in experimental studies [4], it is necessary to explore the influence of short-term plasticity of inhibitory autapses on spike-timing precision of inhibitory interneurons.

Use of AI tools declaration

The authors declare that they have not used Artificial Intelligence (AI) tools in the creation of this article.

Acknowledgments

Conflict of interest

The authors declare there are no conflicts of interest.

References

1. K. W. Latimer, J. L. Yates, M. L. R. Meister, A. C. Huk, J. W. Pillow, Single-trial spike trains in parietal cortex reveal discrete steps during decision-making, *Science*, **349** (2015), 184–187. https://doi.org/10.1126/science.aaa4056
2. A. A. Faisal, L. P. J. Selen, D. M. Wolpert, Noise in the nervous system, *Nat. Rev. Neurosci.*, **9** (2008), 292–303. https://doi.org/10.1038/nrn2258
3. P. Tiesinga, J. Fellous, T. J. Sejnowski, Regulation of spike timing in visual cortical circuits, *Nat. Rev. Neurosci.*, **9** (2008), 97–107. https://doi.org/10.1038/nrn2315
4. A. Bacci, J. R. Huguenard, Enhancement of spike-timing precision by autaptic transmission in neocortical inhibitory interneurons, *Neuron*, **49** (2006), 119–130. https://doi.org/10.1016/j.neuron.2005.12.014

5. H. Sun, H. Zhang, A. Ross, T. T. Wang, A. Al-Chami, S. H. Wu, Developmentally regulated rebound depolarization enhances spike timing precision in auditory midbrain neurons, *Front. Cell. Neurosci.*, **14** (2020). https://doi.org/10.3389/fncel.2020.00236

6. Z. Yang, Q. Tan, D. Cheng, L. Zhang, J. Zhang, E. Gu, The changes of intrinsic excitability of pyramidal neurons in anterior cingulate cortex in neuropathic pain, *Front. Cell. Neurosci.*, **12** (2018). https://doi.org/10.3389/Fncel.2018.00436

7. N. Hajos, J. Palhalmi, E. O. Mann, B. Nemeth, O. Paulsen, T. F. Freund, Spike timing of distinct types of GABAergic interneuron during hippocampal gamma oscillations in vitro, *J. Neurosci.*, **24** (2004), 9127–9137. https://doi.org/10.1523/Jneurosci.2113-04.2004

8. P. Antonoudiou, Y. L. Tan, G. Kontou, A. L. Upton, E. O. Mann, Parvalbumin and somatostatin interneurons contribute to the generation of hippocampal gamma oscillations, *J. Neurosci.*, **40** (2020), 7668–7687. https://doi.org/10.1523/Jneurosci.0261-20.2020

9. P. J. Kammermeier, Endogenous momer proteins regulate metabotropic glutamate receptor signaling in neurons, *J. Neurosci.*, **28** (2008), 8560–8567. https://doi.org/10.1523/Jneurosci.1830-08.2008

10. V. Szegedi, M. Paizs, J. Baka, P. Barzo, G. Molnar, G. Tamas, et al., Robust perisomatic GABAergic self-innervation inhibits basket cells in the human and mouse supragranular neocortex, *Elife*, **9** (2020), 51691. https://doi.org/10.7554/eLife.51691

11. R. A. Tikidji-Hamburyan, J. J. Martinez, J. A. White, C. C. Canavier, Resonant interneurons can increase robustness of gamma oscillations, *J. Neurosci.*, **35** (2015), 15682–15695. https://doi.org/10.1523/Jneurosci.2601-15.2015

12. J. Ma, X. Song, W. Jin, C. Wang, Autapse-induced synchronization in a coupled neuronal network, *Chaos, Solitons Fractals*, **80** (2015), 31–38. https://doi.org/10.1016/j.chaos.2015.02.005

13. E. Yilmaz, M. Ozer, V. Baysal, M. Perc, Autapse-induced multiple coherence resonance in single neurons and neuronal networks, *Sci. Rep.*, **6** (2016), 30914. https://doi.org/10.1038/Srep30914

14. D. Guo, S. Wu, M. Chen, M. Perc, Y. Zhang, J. Ma, et al., Regulation of irregular neuronal firing by autaptic transmission, *Sci. Rep.*, **6** (2016), 26096. https://doi.org/10.1038/Srep26096

15. X. Yang, Y. Yu, Z. Sun, Autapse-induced multiple stochastic resonances in a modular neuronal network, *Chaos*, **27** (2017), 083117. https://doi.org/10.1063/1.4999100

16. C. Yao, Z. He, T. Nakano, Y. Qian, J. Shuai, Inhibitory-autapse-enhanced signal transmission in neural networks, *Nonlinear Dyn.*, **97** (2019), 1425–1437. https://doi.org/10.1007/s11071-019-05060-z

17. L. Li, Z. G. Zhao, Inhibitory autapse with time delay induces mixed-mode oscillations related to unstable dynamical behaviors near subcritical Hopf bifurcation, *Electron. Res. Arch.*, **30** (2022), 1898–1917. https://doi.org/10.3934/era.2022096

18. Z. Zhao, L. Li, H. Gu, Y. Gao, Different dynamics of repetitive neural spiking induced by inhibitory and excitatory autapses near subcritical Hopf bifurcation, *Nonlinear Dyn.*, **99** (2020), 1129–1154. https://doi.org/10.1007/s11071-019-05342-6

19. C. Qi, Y. Li, H. Gu, Y. Yang, Nonlinear mechanism for the enhanced bursting activities induced by fast inhibitory autapse and reduced activities by fast excitatory autapse, *Cogn. Neurodyn.*, **17** (2023), 1093–1113. https://doi.org/10.1007/s11571-022-09872-5

20. X. Ding, H. Gu, Y. Li, Y. Jia, Paradoxical roles of inhibitory autapse and excitatory synapse in formation of counterintuitive anticipated synchronization, *Chin. Phys. B.*, **32** (2023), 088701. https://doi.org/10.1088/1674-1056/Acc450

21. Y. Jia, H. Gu, Y. Li, X. Ding, Inhibitory autapses enhance coherence resonance of a neuronal network, *Commun. Nonlinear Sci. Numer. Simul.*, **95** (2021), 105643. https://doi.org/10.1016/J.Cnsns.2020.105643

22. Y. Jia, H. Gu, Y. Li, Influence of inhibitory autapses on synchronization of inhibitory network gamma oscillations, *Cogn. Neurodyn.*, **17** (2023), 1131–1152. https://doi.org/10.1007/s11571-022-09856-5

23. E. M. Izhikevich, Neural excitability, spiking and bursting, *Int. J. Bifurcation Chaos*, **10** (2000), 1171–1266. https://doi.org/10.1142/S0218127400000840

24. J. Mikiel-Hunter, V. Kotak, J. Rinzel, High-frequency resonance in the gerbil medial superior olive, *Plos Comput. Biol.*, **12** (2016), 1005166. https://doi.org/10.1371/journal.pcbi.1005166

25. X. Ding, H. Gu, B. Jia, Y. Li, Anticipated synchronization of electrical activity induced by inhibitory autapse in coupled Morris-Lecar neuron model, *Acta. Phys. Sin.*, **70** (2021), 218701. https://doi.org/10.7498/Aps.70.20210912

26. B. Jia, H. Gu, Identifying type I excitability using dynamics of stochastic neural firing patterns, *Cogn. Neurodyn.*, **6** (2012), 485–497. https://doi.org/10.1007/s11571-012-9209-x

27. B. Jia, H. Gu, Dynamics and physiological roles of stochastic firing patterns near bifurcation points, *Int. J. Bifurcation Chaos*, **27** (2017), 1750113. https://doi.org/10.1142/S0218127417501139

28. X. Wang, Neurophysiological and computational principles of cortical rhythms in cognition, *Physiol. Rev.*, **90** (2010), 1195–1268. https://doi.org/10.1152/physrev.00035.2008

29. C. Borgers, *An Introduction to Modeling Neuronal Dynamics*, Springer, Cham, 2017. https://doi.org/10.1007/978-3-319-51171-9

30. X. Wang, G. Buzsaki, Gamma oscillation by synaptic inhibition in a hippocampal interneuronal network model, *J. Neurosci.*, **17** (1996), 6402–6413. https://doi.org/10.1523/jneurosci.16-20-06402.1996

31. B. Ermentrout, *Simulating, Analyzing, and Animating Dynamical Systems: A Guide to XPPAUT for Researchers and Students*, SIAM, Philadelphia, 2002. https://doi.org/10.1137/1.9780898718195

32. C. Deleuze, G. S. Bhumbra, A. Pazienti, J. Lourenco, C. Mailhes, A. Aguirre, et al., Strong preference for autaptic self-connectivity of neocortical PV interneurons facilitates their tuning to gamma-oscillations, *PLoS Biol.*, **17** (2019), 3000419. https://doi.org/10.1371/journal.pbio.3000419

33. A. Bacci, J. R. Huguenard, D. A. Prince, Functional autaptic neurotransmission in fast-spiking interneurons: A novel form of feedback inhibition in the neocortex, *J. Neurosci.*, **23** (2003), 859–866. https://doi.org/10.1523/jneurosci.23-03-00859.2003